ORIGINAL PAPER

A multi-segment alpha shape-based continuum method for long-term density propagation with bifurcation

Pan Sun · **Shuang Li** · **Mirko Trisolini** · **Camilla Colombo**

Abstract This paper studies the bifurcation case for the planar phase space long-term density propagation problem, and presents an improved multi-segment continuum method for accurate and efficient long-term density propagation, by introducing the multi-segment method to the alpha shape triangulation-based linear interpolation method. The density evolution equation is formulated for the continuum density propagation under the influence of the solar radiation pressure and Earth's oblateness using semi-analytical equations. For the overall highly deformed and elongated density distribution for the bifurcation case, the multi-segment method is introduced to the alpha shape-based linear interpolation method to get accurate interpolated density, by dividing the overall density distribution into multiple segments and performing the linear interpolation within the actual non-convex hull of the sample distribution for each segment. Four segments are divided for the overall density distribution considering the Hamiltonian dynamic constraints on the solar angle domain. The superiority of the improved multi-segment alpha shape-based continuum method is demonstrated for accurate and efficient density propagation for the bifurcation case in the context of the high-altitude and high area-to-mass ratio satellite long-term propagation.

Keywords Density evolution equation · Alpha shape · Linear interpolation · Bifurcation · Multi-segment method

Shuang Li: Member AIAA.

P. Sun
Department of Intelligent Equipment, Changzhou College of Information Technology, Changzhou, China
e-mail: sunpan@czcit.edu.cn

S. Li (✉)
Advanced Space Technology Laboratory, College of Astronautics, Nanjing University of Aeronautics and Astronautics, Nanjing, China
e-mail: lishuang@nuaa.edu.cn

M. Trisolini · C. Colombo
Department of Aerospace Science and Technology, Polytechnic University of Milan, Milan, Italy
e-mail: mirko.trisolini@polimi.it

C. Colombo
e-mail: camilla.colombo@polimi.it

1 Introduction

The long-term density propagation problem is studied in many applications: the dynamic evolution of the interplanetary dust [8, 9], nanosatellite constellations [18], the global space debris population [19, 21], swarms of high area-to-mass ratio spacecraft [1], the asteroid post-encounter motion [27], small-debris-object clouds [5, 15–17], and clouds of high altitude and high area-to-mass ratio satellites [22–24, 26]. To achieve accurate density propagation after long-term

propagations, an accurate and efficient characterisation for the highly nonlinear density is required.

Monte Carlo (MC) is a traditional method for density propagation. It provides reference density via a large number of random samples, but at the cost of a high computational load. To reduce the computational load, many nonlinear methods are developed for density propagation. In [10], the authors classify the methods into two categories: parametric (where one evolves the statistical moments) and nonparametric (where one approximates or directly propagates the evolution equation of the Probability Density Function (PDF)). Representative nonparametric methods are Gaussian Mixture Model (GMM)-based hybrid methods, such as Gaussian Mixture Model-Unscented Transformation (GMM-UT) [6], Density Evolution Equation (DEE, or continuity equation) [18, 22, 24, 25]. The former approximates the non-Gaussian PDF at any time using the weighted sum of the first two statistical moments of the Gaussians. The latter directly propagates the density as a fluid with continuous properties, and can be solved together with the propagation of the state space via the method of characteristics [2, 10, 22]. Since all the statistical moments can be derived from the PDF, with the nonparametric methods, we get all the density information at any time via the evolved PDF.

For the density propagation problem featuring the highly deformed and elongated density distribution after long-term propagations, to get accurate density in an efficient way, many practical techniques are applied within different method frameworks [4, 13, 23, 27]. For example, for highly nonlinear problems, as shown by [4, 27], the introduction of the domain splitting improves the density accuracy of the Differential Algebra (DA) method by subdividing the initial larger density domain into smaller subdomains. When tackling the long-term density propagation problem featuring highly deformed and elongated density distribution within the GMM framework, as shown by [23], hybrid Gaussian Mixture splitting techniques combining both the initial multidirectional splitting and adaptive splitting during the propagation, are necessary for the accurate density propagation, by allowing the smaller density domains for Gaussians both at the initial time and during the density propagation. Overall, the main idea of these practical techniques is to reduce the overall larger density domain to multiple smaller density domains for improved density accuracy after long-term propagations.

The DEE method has been developed over the years. Different from the MC method (where many simulations are conducted for an equivalent large number of random samples), we can get the density evolution of the entire clouds of objects through a finite number of simulations for a finite number of random samples, featuring a much lower computational load. The accuracy of the DEE method mainly depends on the dynamic nonlinearity, the performance of the interpolation method, and the binning method. In the work of [22], the DEE method and the Gaussian mixture model are compared for the Medium Earth Orbit (MEO) planar phase space long-term density propagation problem in the context of high-altitude and high area-to-mass ratio satellite long-term propagation. It demonstrates the overall good performance of the DEE method for accurate density propagation within different phase space domains. However, when the phase space is highly deformed and elongated, the density accuracy of the case with fewer samples is low. This is because, when the density distribution is highly deformed and elongated, the actual density distribution is not convex. The Delaunay Triangulation-based Binning method adopted in [22] (defined as DT-B1) performs worse because it interpolates the density within the whole convex hull. In this case, the core value and the overall distribution characteristic of the joint density, and the peaks of the marginal density in two phase space directions (eccentricity and solar angle) are underestimated. To solve this problem within the continuum method framework, in the work of [24], the authors present an improved alpha shape-based linear interpolation method and an improved binning method (defined as AT-B2) for accurate and efficient density propagation. Different from the Delaunay triangulation-based linear interpolation method (DT), the improved alpha shape triangulation-based linear interpolation method (AT) is used to obtain linearly interpolated density within the actual non-convex hull enclosing all the samples. The improved binning method (B2) increases the density accuracy by considering the weight for each alpha shape triangulation per bin area, and the variant nonlinearity of the density within each alpha shape triangulation. However, these previous works have been limited to the non-bifurcation cases [22, 24], i.e., the study for the long-term density evolution is limited within each sub-phase space domain. They do not consider the cases when the phase space evolution

passes through the bifurcation point. Since the dynamic characteristics change quickly and greatly near the bifurcation point, as we can infer in the previous works, the higher density nonlinearity with higher deformation and elongation will occur for the bifurcation case after long-term propagations. Thus, it is of greater interest and higher difficulty to understand how the phase space and its associated density evolve with time for the bifurcation case.

A major contribution of the current work is that a Multi-Segment (MS) method is introduced to the AT method to improve the accuracy for characterising the highly deformed and elongated density distribution for the bifurcation case. The MS method implemented in the current paper is to first divide the overall highly deformed and elongated density distribution into four segments on the solar angle domain by considering the Hamiltonian dynamic constraints. Then apply the alpha shape-based linear interpolation within the actual non-convex hull of the sample distribution for each segment. In this case, we can achieve improved interpolated density for the less deformed and elongated density space for each segment, and thus further improve the interpolation accuracy for the alpha shape-based linear interpolation method. The B2 binning method is used for density calculation. In this paper, we define the combination of the MS method, the AT method and the B2 method as the multi-segment alpha shape-based continuum method (called MAT-B2). The combination of the MS method and the AT method is defined as the multi-segment alpha shape triangulation-based linear interpolation method (called MAT). Using the previous works as a benchmark [22, 24], the MEO planar phase space case subject to the semi-analytical coupled effects of the solar radiation pressure and Earth's oblateness is given, for demonstrating the improved performance in the density accuracy and the computational efficiency for the MAT-B2 method, for the bifurcation case for the long-term density propagation problem.

The paper is organised as follows. Section 2 gives the problem formulation and analysis, including the semi-analytical equation, the density evolution equation, the long-term density propagation problem with bifurcation. Section 3 presents the MAT-B2 method, together with the computation procedure for solving the density propagation problem with the MAT-B2 method. In Section 4, the simulation setup is given, including the definition of the initial conditions for the

MEO planar phase space case, and the definition of the accuracy measure. Section 5 presents the density propagation results for the test case, and gives some discussion on the superiority of the MAT-B2 method for accurate and efficient density propagation for the bifurcation case for the highly deformed and elongated density distribution. Section 6 gives some conclusions.

2 Problem formulation and analysis

In this paper, we will focus on studying the bifurcation case for the planar phase space long-term density propagation problem within the continuum method framework, and improving the density accuracy for the bifurcation case for the highly deformed and elongated density distribution using the improved MAT-B2 method. To study the phase space evolution together with its associated density for the bifurcation case, in this section, we first present the semi-analysed dynamic equations for the MEO planar phase space evolution under the influence of Solar Radiation Pressure (SRP) and Earth's oblateness (J_2), and formulate the associated density evolution equation. Then, we give an insight into the bifurcation case for the long-term density propagation problem.

2.1 Semi-analytical equation

The evolution equation of the dynamic system subject to the semi-analysed coupled effect of the Earth's oblateness and the solar radiation pressure is [14]

$$\dot{x}(t) = \begin{bmatrix} \dfrac{\mathrm{d}e}{\mathrm{d}t} \\ \dfrac{\mathrm{d}\phi}{\mathrm{d}t} \end{bmatrix}$$
$$= \begin{bmatrix} n_s \left(C\sqrt{1-e^2} \sin\phi \right) \\ n_s \left(C\dfrac{\sqrt{1-e^2}}{e}\cos\phi + \dfrac{W}{(1-e^2)^2} - 1 \right) \end{bmatrix}$$
(1)

where $\boldsymbol{x} = [e; \phi]$ (eccentricity; solar angle) is the state vector to describe the planar equatorial orbit, n_s is the mean motion of the sun, and C and W represent the dimensionless radiative and oblateness parameters, respectively. It should be noted that the solar angle

represents the angular distance between the pericentre and the direction towards the sun [22].

For Eq. (1), it can be rewritten in the quasi-canonical form as follows [11, 12],

$$
\begin{cases}
\dfrac{\mathrm{d}e}{\mathrm{d}t} = n_s \left(-\dfrac{\sqrt{1-e^2}}{e} \dfrac{\partial H}{\partial \phi} \right) \\[3mm]
\dfrac{\mathrm{d}\phi}{\mathrm{d}t} = n_s \left(\dfrac{\sqrt{1-e^2}}{e} \dfrac{\partial H}{\partial e} \right)
\end{cases}
\tag{2}
$$

where H is the phase space Hamiltonian, $H = (1-e^2)^{1/2} + Ce\cos\phi + (W/3)\cdot(1-e^2)^{-3/2}$. $H(e, \phi) = $ constant, which means for a phase space variable pair (e, ϕ) defined at time t, the phase space evolution is along a constant Hamiltonian contour line.

To study the phase space structure, we can calculate the stationary points for the Hamiltonian H by solving for $\partial H/\partial e = \partial H/\partial \phi = 0$. Summarised results for stationary points constrained to the planar problem are shown in [14], while solutions extended to non-planar orbits can be found in [7].

Here we assume $C = 0.15$, $W = 0.409$, and $a = 2.5\ R_E$, corresponding to the phase portrait of type III in Fig. 1 in [22], where a is the semimajor axis, R_E is the equatorial radius of Earth, and a is treated as constant as no eclipses are considered in this paper. Figure 1 shows the phase portrait of type III (including five stationary points P_i, $i \in \{1,2,\cdots,5\}$), and the three sub-phase space domains $SubD_i$, $i \in \{1,2,3\}$ in Fig. 1 in [22]. The horizontal line marks the critical eccentricity $e_{cri} = 0.6$ for Earth reentry at the Earth surface. As we can see in Fig. 1, in this phase portrait, the bifurcation is detected at the

stationary point P_4. The Hamiltonian phase space is divided into three sub-phase space domains [22] departed by the contour lines passing through the stationary points P_1 and P_4. As shown in Fig. 1b, the three sub-domains reside between the Hamiltonian contour lines H_{P5} and H_{P1}, H_{P1} and H_{P4}, H_{P4} and H_{P3}, respectively. When the phase space initial conditions $x_0 = [e_0, \phi_0]$ are chosen within the sub-domain $SubD_1$ or $SubD_2$, i.e., $H(e_0, \phi_0) < H_{P4}$, it is possible to reach the critical eccentricity $e_{cri} = 0.6$ for Earth reentry after long-term propagations, while when they are chosen within the sub-domain $SubD_3$, i.e., $H(e_0, \phi_0) > H_{P4}$, it is impossible to reach the critical eccentricity after long-term propagations. This means dramatic orbital changes can be made under small variations of initial data [14], and ultimately Earth reentry may be achieved. The dramatic orbital changes due to the stationary point P_4 is called bifurcation. In [22], they study the non-bifurcation case for the long-term planar phase space density propagation problem; when the phase space is highly deformed and elongated, the density accuracy for the case with fewer samples is low. Since the dynamic characteristics change quickly and greatly near the bifurcation point, and different nonlinearity is shown within different sub-domains after long-term propagations [22], it is of greater interest and higher difficulty, to understand how the phase space and its associated density evolve with time for the bifurcation case within two different sub-domains, $SubD_3$ and $SubD_2$. As we can infer in [22], compared with the non-bifurcation case in [22], greater density nonlinearity with higher deformation and elongation will occur for
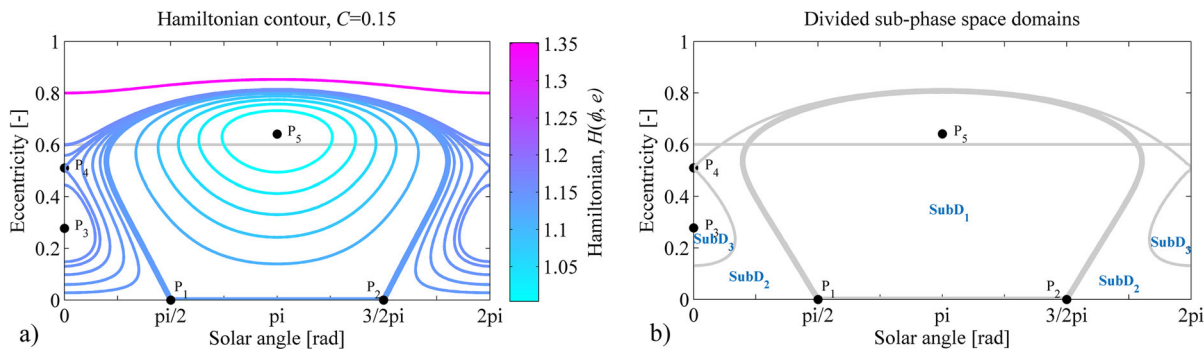

Fig. 1 **a** Phase portrait of type III; **b** Divided sub-phase space domains ($a = 2.5\ R_E$, $W = 0.409$, $C = 0.15$, critical eccentricity $e_{cri} = 0.6$ for Earth reentry) [22]

the bifurcation case after long-term propagations subject to nonlinear dynamics within two different sub-domains when passing through the bifurcation point.

To give a preliminary insight into the long-term phase space evolution problem with bifurcation, Fig. 2 shows the initial sample distribution at time $t = 0$ within the phase space portrait for the bifurcation case, and the phase space evolution results at times $t = \{0, 0.5, 1, 1.5, 2\}$ years, with the initial conditions in terms of the mean $\boldsymbol{m}_0 = [e_0; \phi_0] = [0.245, 0.4495]$, the covariance matrix $\boldsymbol{P}_0 = \text{diag}\{6.25\text{E}{-}4, 0.0096\}$, and the sample number $N_{sam} = 1\text{E}5$ of the initial Gaussian distribution. The two gray half-closed loop arcs in Fig. 2b denote the minimum (the lower one) and the maximum Hamiltonian contour line for the phase space random samples. Note that here the initial conditions for the Gaussian samples are specified to make sure of the realisation of the long-term density propagation within two sub-phase space domains that include the bifurcation point P4, i.e., SubD3 and SubD2 (see Fig. 2a). As expected, we can see in Fig. 2 that for the bifurcation case, the deformation of the phase space distribution increases with time within two sub-domains. At times $t = \{1.5, 2\}$ years when passing through the bifurcation point P4, the highly deformed and elongated phase space distribution even extends within the whole solar angle domain, exhibiting higher nonlinearity. In this paper, we will focus on studying the bifurcation case for the long-term density propagation problem, and improving the density accuracy

for the bifurcation case for the highly deformed and elongated density distribution using an improved multi-segment alpha shape-based continuum method.

2.2 Density evolution equation

To study the density evolution in the phase space within the continuum method framework, we need to propagate density evolution equation together with the state space dynamics (see Eq. (1)).

Assume that n is the density to be solved for the nonlinear dynamics. Given m generic variables x_i, $i \in \{1, \cdots, m\}$, and assuming that the density is differentiable for all x_i, the density evolution equation is written as follows [5, 8, 16, 18, 22]

$$\frac{\partial n}{\partial t} + \frac{\partial n}{\partial x_1} v_1 + \cdots + \frac{\partial n}{\partial x_m} v_m + \left[\frac{\partial v_1}{\partial x_1} + \cdots + \frac{\partial v_m}{\partial x_m} \right] n = \dot{n}^+ - \dot{n}^-$$

(3)

where $\dot{n}^+ - \dot{n}^-$ is the discontinuous acceleration terms included for the dynamic system, such as the random maneuver correction on the topic of satellite end-of-life disposal, v_i is the ith component of the continuous acceleration terms, $v_i = \mathrm{d}x_i/\mathrm{d}t$ (see Eq. (1)). In this paper, no discontinuous acceleration terms are considered, i.e., $\dot{n}^+ - \dot{n}^- = 0$. By applying the method of characteristics [2], the following equations are obtained [16],
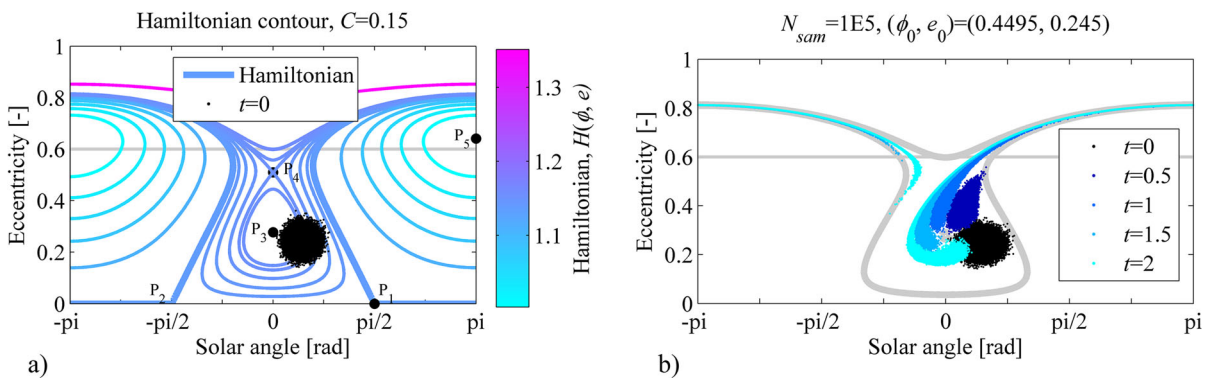

Fig. 2 **a** Phase portrait of type III and the initial sample distribution at time $t = 0$ for the bifurcation case; **b** Long-term phase space dynamic evolution at times $t = \{0, 0.5, 1, 1.5, 2\}$ years ($a = 2.5\ R_E$, $W = 0.409$, $C = 0.15$, $N_{sam} = 1\text{E}5$, critical eccentricity $e_{cri} = 0.6$ for Earth reentry)

$$\begin{cases} \dfrac{\mathrm{d}t}{\mathrm{d}u} = 1 \\[2mm] \dfrac{\mathrm{d}x_1}{\mathrm{d}u} = v_1(x_1, \cdots, x_m) \\[2mm] \vdots \\[2mm] \dfrac{\mathrm{d}x_m}{\mathrm{d}u} = v_m(x_1, \cdots, x_m) \\[2mm] \dfrac{\mathrm{d}n}{\mathrm{d}u} = -\left[\dfrac{\partial v_1}{\partial x_1} + \cdots + \dfrac{\partial v_m}{\partial x_m}\right] n(x_1, \cdots, x_m, t) \end{cases} \tag{4}$$

where u is a parametrisation of the characteristic lines. From Eq. (4), we can see that given the specific formulation for the dynamic system (i.e., given the actual expressions of v_i), the time evolution of the density $n(x_1, \cdots, x_m, t)$ can be obtained together with the state space variables x_i.

For the case in examination, to get the density together with the state space, the density evolution equation for the associated dynamic system (see Eq. (1)) is calculated as,

$$\frac{\mathrm{d}n}{\mathrm{d}t} = -\left(\frac{\partial}{\partial e}\left(\frac{\mathrm{d}e}{\mathrm{d}t}\right) + \frac{\partial}{\partial \phi}\left(\frac{\mathrm{d}\phi}{\mathrm{d}t}\right)\right)n = \frac{C \cdot n_s \cdot \sin\phi}{e\sqrt{1-e^2}}n \tag{5}$$

2.3 Long-term density propagation problem with bifurcation

For the case in examination, to obtain the propagated density (i.e., the non-Gaussian PDF, $p_t(\boldsymbol{x})$) for the DEE method at any time t, the following three steps are required. First, generate initial random samples with a predefined sample number N_{sam} subject to the initial PDF $p_{t_0}(x)$, and calculate the initial density weights $n(e, \phi, t_0)$ for the samples at time t_0. Thus, initial samples in the 2D state space (e, ϕ) and their associated density weights are obtained in the 3D extended state space (e, ϕ, n). Note that for the DEE method the selection of the sample number N_{sam} is important, because it influences the density accuracy and the whole computation time. Second, integrate the density evolution equation (see Eq. (5)) together with the state space dynamics (see Eq. (1)) to obtain the propagated samples and the associated density weights in the 3D extended state space. Third, calculate the density by processing the final samples and density weights in a statistical way. In this paper, the linear interpolation

method is combined with the binning method to calculate the density.

To give a preliminary insight into the long-term density propagation problem with bifurcation, here we refer to the work of [22], and test the performance of the DT-B1 method compared with that of the MC method. Note that the DT-B1 method is the Delaunay triangulation-based binning method adopted in [22]. To complement the accuracy analysis for the DT-B1 method with respect to that of the MC method, a MC simulation is performed. The number of MC samples is set to be N_{sam} = 1E5 because it ensures the convergence of the MC method and avoids the higher computational load for a test with a larger sample number. The same sample number N_{sam} = 1E5 as that of the MC method is set for the DT-B1 method to compare the accuracy of the DT-B1 method with the MC method for the bifurcation case.

Figure 3 shows the joint density evolution for the bifurcation case (corresponding to the phase space evolution in Fig. 2b) at times t = {0, 0.5, 1, 1.5, 2} years for the MC and DT-B1 method, where dt gives the time interval between two consecutive snapshots, dt = 0.5 yr. Figure 4 gives the marginal density evolution for the bifurcation case at times t = {0, 0.5, 1, 1.5, 2} years for the MC and DT-B1 method. From Figs. 3 and 4 for the MC method, we can see that high nonlinearity is shown in the joint and marginal density after long-term propagations when passing through the bifurcation point P_4, i.e., at times t = {1.5, 2} years. The higher nonlinearity is shown for the marginal density of the eccentricity in two local density peaks and the highly deformed distribution characteristic than that for the marginal density of the solar angle. As we can see in Fig. 3 and, for the DT-B1 method, for a large sample number case N_{sam} = 1E5 as that of the MC method, it fails to capture the high nonlinearity in the joint and marginal density for the bifurcation case at times t = {1.5, 2} years. Note that for the DT-B1 method, only the case result of a larger sample number N_{sam} = 1E5 (i.e., DEE-1E5) is presented. We do not give the case result for a smaller sample number, because only the worse density is got at times t = {1.5, 2} years than that of the case N_{sam} = 1E5. Similar to the non-bifurcation case in [22], the DT-B1 method works fine in capturing the joint and marginal density when the phase space is not highly deformed and elongated at times t = {0, 0.5, 1} years.
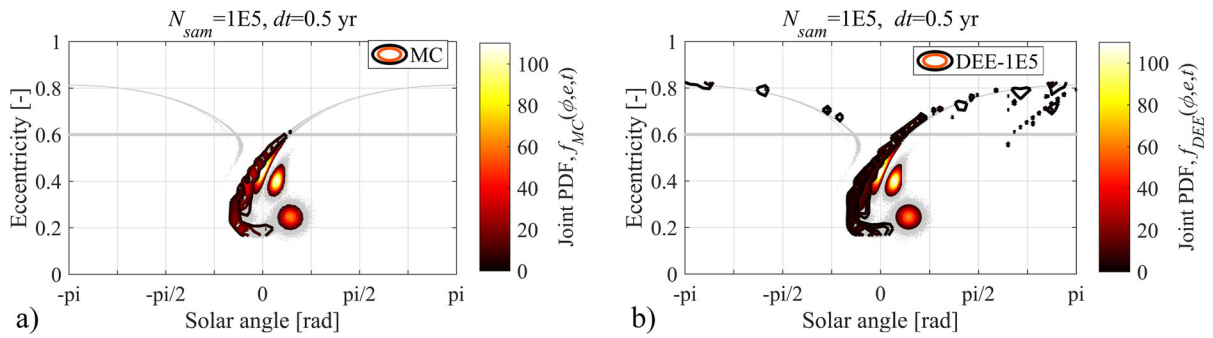
Fig. 3 Joint density evolution at times $t = \{0, 0.5, 1, 1.5, 2\}$ years for the bifurcation case, MC versus DT-B1 (DEE-1E5)
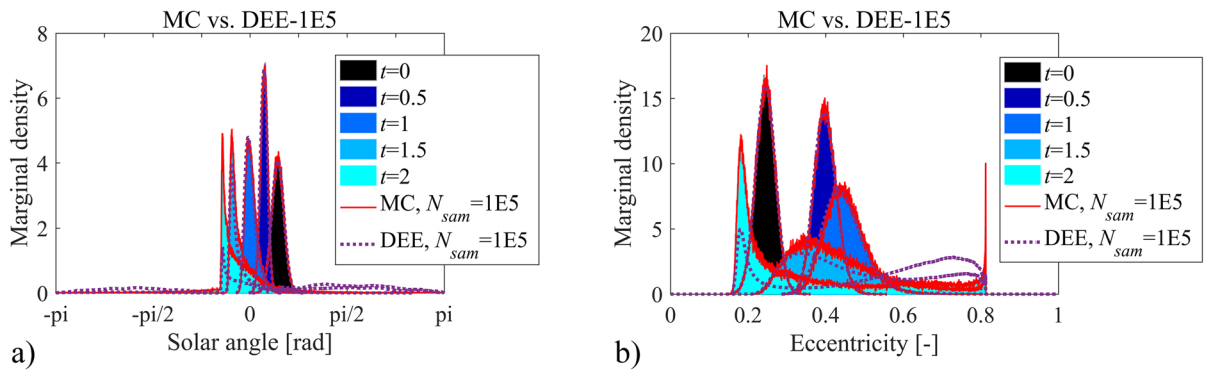

Fig. 4 Marginal density evolution at times $t = \{0, 0.5, 1, 1.5, 2\}$ years for the bifurcation case, MC versus DT-B1 (DEE-1E5)

Overall, from Figs. 3 and 4, we can conclude that for the bifurcation case when passing through the bifurcation point P_4, i.e., at times $t = \{1.5, 2\}$ years, the density accuracy for the DT-B1 method is low. It fails to capture the high nonlinearity for the joint density and the marginal density in two phase space directions, including the core value for the joint density, the overall distribution characteristics of the joint and marginal density, and the density peaks for the marginal density in two phase space directions. This is because, when the density distribution is highly deformed and elongated, the actual density distribution is not convex. The DT-B1 method performs worse because it interpolates the density within the whole convex hull. The B1 method calculates the joint and marginal density as the weighted mean of density weights per bin area and per bin width, respectively. It does not include the variant nonlinearity within each Delaunay triangulation for density calculation. In this paper, we will focus on improving the density accuracy for the bifurcation case for the highly deformed and elongated density distribution using an

improved multi-segment alpha shape-based continuum method.

3 Improved multi-segment alpha shape-based continuum method

To improve the density accuracy for the bifurcation case for the highly deformed and elongated density distribution, we present an improved method called MAT-B2, which is combined by the MS method (presented in this paper) and the AT-B2 method (presented by [24]). In this section, we first introduce the MAT method and the B2 binning method, respectively. Then the whole procedure for solving the bifurcation case for the planar phase space long-term density propagation problem with the MAT-B2 method is presented.

3.1 The proposed MAT interpolation method

To improve the interpolation accuracy for the bifurcation case for the highly deformed and elongated

density distribution, this paper proposes the MAT interpolation method, by introducing the MS method to the AT interpolation method. Here we will present the AT method, and the MS method, respectively, to illustrate the MAT method.

3.1.1 AT interpolation method

For the AT method, the concept of alpha shape is included to get accurate interpolated density within the non-convex hull enclosing all the samples. Different from the DT method, which is done within the whole convex hull of the scattered samples, the AT method helps adapt to the evolution of the shape of the state space volume.

Here we present the computation procedure for performing the linear interpolation using the alpha shape triangulation. Assume a generic 2D problem in two independent variables x_i, $i \in \{1,2\}$, the N_{sam} propagated samples and their associated density weights at any time t in the vectors $(x_{10}, x_{20}, n_0(x_{10}, x_{20}, t))$, and the grid number $Ngrid$ for each dimension for performing the linear interpolation. To get the alpha shape-triangulation-based interpolated density, three steps are required. First, perform the Delaunay triangulation-based interpolation for the specified query points (x_1, x_2) [24, 25],

$$n(x_1, x_2, t) = \sum_{i=1}^{V} n_i B_i(x_1, x_2) \tag{6}$$

where $n(x_1, x_2, t)$ is the Delaunay triangulation-based linear interpolated density of the point (x_1, x_2), V is the number of vertices of the simplex for the Delaunay triangulation, n_i is the value of the density for the ith vertex, $B_i(x_1, x_2)$ is the barycentric coordinates of the ith vertex including the point (x_1, x_2). As we can see in Eq. (6), if we find the barycentric coordinates of the vertices, the linear interpolation can be done. The main advantage of the DT method is the capability of retaining the scattered samples at the nodes of the triangulation [20]. Theoretically, the larger the sample number N_{sam}, the better the density quality for the DT method. Second, generate the compact alpha shape triangulation within the actual non-convex hull enclosing all the scattered sample data for a predefined alpha radius r_a [3, 24, 25],

$$As = \{A_i(x_{10}, x_{20}, r_a), i \in \{1, 2, \cdots, V_A\} | A_i \\ \subseteq D(x_{10}, x_{20})\} \tag{7}$$

where As is the generated alpha shape triangulation, A_i is the ith vertex of the simplex for the alpha shape triangulation, V_A is the number of vertices of the simplex for the alpha shape triangulation, $D(x_{10}, x_{20})$ is the Delaunay triangulation for the samples (x_{10}, x_{20}). As we can see in Eq. (7), the generated alpha shape triangulation is the subset of the Delaunay triangulation. The alpha shape is introduced to remove the surplus vertices of the simplex generated when the shape of the density distribution is not convex. Note that the selection of the alpha radius r_a is important, as it decides how accurate the alpha shape triangulation characterises the actual shape of the density distribution. In this paper, we check different r_a values using the dichotomy, and determine the most appropriate for the test cases in examination. In principle, also in this case, the larger the sample number N_{sam}, the better the returned alpha shape triangulation is at characterising the evolved shape of the density space. Third, retain all the Delaunay triangulation-based interpolated results that are inside or make up the alpha shape triangulation, and perform the alpha shape triangulation-based linear interpolation [24, 25],

$$n_a(x_1, x_2, t) = \sum_{i=1}^{V_A} n_{ai} B_{ai}(x_1, x_2) \tag{8}$$

where $n_a(x_1, x_2, t)$ is the alpha shape triangulation-based linear interpolated density of the point (x_1, x_2), n_{ai} is the value of the density for the ith vertex for the alpha shape triangulation, $B_{ai}(x_1, x_2)$ is the barycentric coordinates of the ith vertex including the point (x_1, x_2) for the alpha shape triangulation.

With the above three steps, we get the improved alpha shape-based linearly interpolated density by retaining the Delaunay triangulation-based interpolated results within the alpha shape triangulation. Note that, the selection of the sample number N_{sam} and the gird number $Ngrid$ is important, because it affects the accuracy of the final interpolated density $n_a(x_1, x_2, t)$, and the computational efficiency. In this paper, we will select the suitable sample number N_{sam} and the grid number $Ngrid$ by trading off the density accuracy and the computational efficiency.

3.1.2 Multi-segment method

To improve the interpolation accuracy for the bifurcation case, here we introduce the MS method to divide the overall highly deformed and elongated density distribution into multiple segments for performing the linear interpolation.

The main idea of the MS method is to divide the highly deformed and elongated density distribution into multiple segments for density interpolation. For the bifurcation case for the highly deformed and elongated density distribution when passing through the bifurcation point P_4 (see Fig. 2b), the density distribution exhibits high deformation and elongation within the whole domain on the solar angle direction, and is greatly departed within two sub-domains divided by the critical Hamiltonian contour line passing through the bifurcation pint P_4 (see Fig. 1). Considering the higher elongation of the density distribution on the solar angle domain than the eccentricity domain, four segments are divided in this paper, for the overall density distribution on the solar angle domain considering the Hamiltonian dynamic constraints.

Assume $Sg = \{Sg_1, Sg_2, Sg_3, Sg_4\}$, where Sg is the ensemble of the propagated samples for the DEE method, and Sg_i, $i \in \{1,2,3,4\}$, is the ith segment after division. The division standard for the divided four segments considering the Hamiltonian dynamics constraints is given as follows,

$$\begin{cases} Sg_1 : H(\mathbf{x}) < H_{P4}, \phi > -\dfrac{\pi}{2} \\ Sg_3 : H(\mathbf{x}) < H_{P4}, \phi > = \dfrac{\pi}{2} \\ Sg_4 : H(\mathbf{x}) < H_{P4}, \phi < -\dfrac{\pi}{2} \\ Sg_2 = Sg - \{Sg_1, Sg_3, Sg_4\} = \{x | x \in Sg, x \notin (Sg_1 \cup Sg_3 \cup Sg_4)\} \end{cases} \tag{9}$$

where $\boldsymbol{x}$ is the state vector for the propagated samples to be interpolated, $H(\boldsymbol{x})$ is the Hamiltonian value of the state vector $\boldsymbol{x}$ for the 2D planar phase space, H_{P4} is the Hamiltonian value for the Hamiltonian contour line passing through the bifurcation point P_4 (see Fig. 1 in Sect. 2.2 in this paper).

From Eq. (9), we can see that, for the case in examination, due to the Hamiltonian dynamic constraint of $H(\boldsymbol{x}) < H_{P4}$, the three segments $\{Sg_1, Sg_3, Sg_4\}$ are all constrained within one sub-domain, $SubD_2$. The other segment Sg_2 is mainly constrained

within the sub-domain $SubD_3$. It should be noted that, the division standard is defined in this paper for the following considerations. First, for the bifurcation case studied in this paper, we only consider the density evolution problem for the highly deformed and elongated density distribution when passing through the bifurcation point P_4 within the two sub-domains $\{SubD_2, SubD_3\}$. Second, as we can see from the results of the non-bifurcation case for the long-term density propagation problem in the work of [22], higher nonlinearity within the sub-domain $SubD_2$ is detected than that within the sub-domain $SubD_3$. For the non-bifurcation case within the sub-domain $SubD_2$, when approaching the eccentricity domain larger than the critical eccentricity $e_{cri} = 0.6$, a low density accuracy is got for the case with fewer samples for the DT-B1 method (see the results at $t = 1.5$ years in Fig. 11 in [22]). To improve the interpolation accuracy for the bifurcation case when passing through the bifurcation point P_4, we divide the overall highly deformed and elongated density distribution into three segments $\{Sg_1, Sg_3, Sg_4\}$ within the sub-domain $SubD_2$, and put the remaining parts into the segment Sg_2 (which is mainly within the sub-domain $SubD_3$) (Fig. 4).

To give an insight into the MS method, Fig. 5 shows the sample distribution ($N_{sam} = 1.6E4$) in the 2D solar angle-eccentricity ($\phi - e$) phase space for the bifurcation case at time $t = 1.5$ years, and its associated divided segments according to the division standard in Eq. (9) (for Sg_1, in yellow; for Sg_2, in green; for Sg_3, in blue; for Sg_4, in black). Note that here the snapshot case at time $t = 1.5$ years corresponds to the bifurcation case shown in Fig. 2 in this paper. As we can see in Fig. 5, compared with the direct processing for the overall highly deformed and elongated density distribution for the bifurcation case, with the introduction of the MS method, the overall deformed and elongated density distribution are divided into multiple segments with the inclusion of the Hamiltonian dynamic constraints. In this case, we can achieve improved interpolated density for the less deformed and elongated density space for each segment (this will be shown in Fig. 6 in this paper). Theoretically, the more divided segments, the lower deformation and elongation for the density space for each segment, and maybe the higher interpolated density accuracy for the overall density distribution. In this paper, we give the four segment division standard
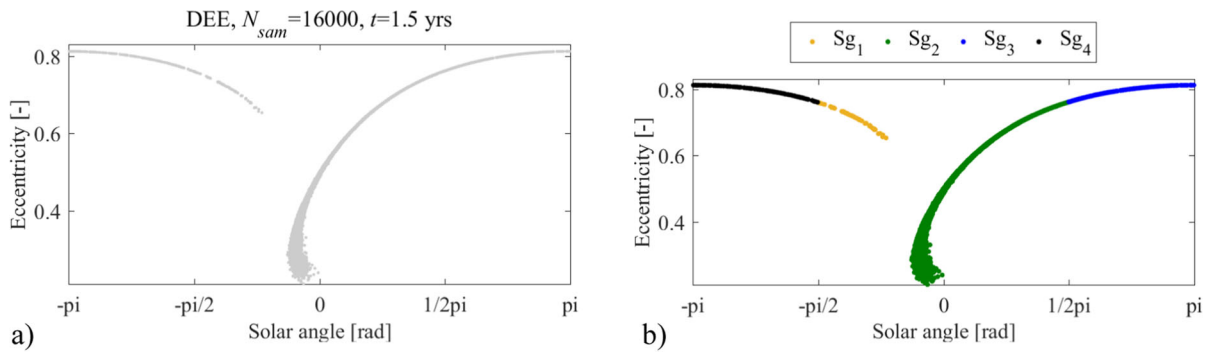
Fig. 5 a Sample distribution at time $t = 1.5$ years for the bifurcation case ($N_{sam} = 1.6E4$, corresponding to the case in Fig. 2 in this paper); **b** Illustration for the technique of the multi-segment method for the MAT method for the bifurcation case at $t = 1.5$ years
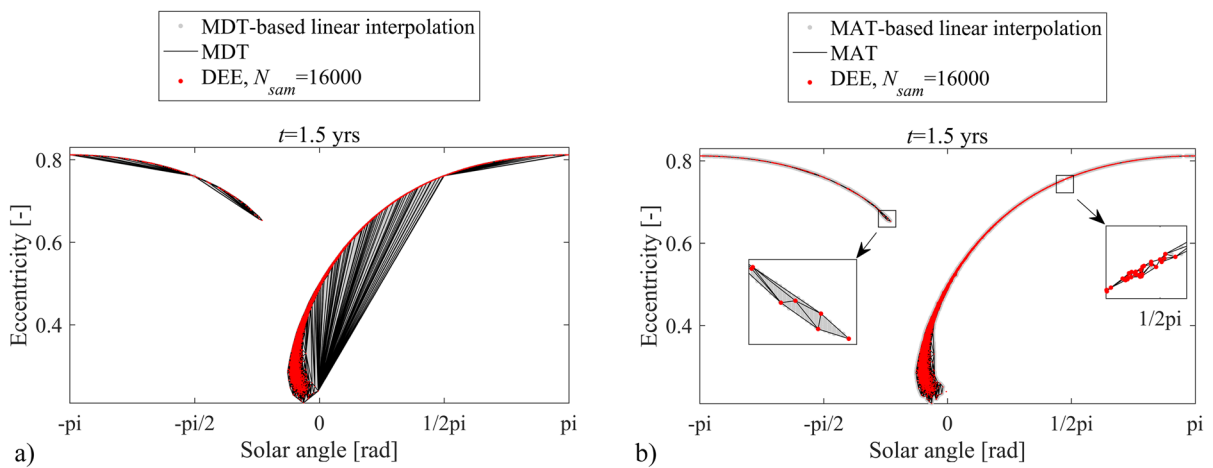

Fig. 6 Illustration and comparison for the **a** MDT-based linear interpolation, **b** MAT-based linear interpolation, at time $t = 1.5$ years for the bifurcation case ($N_{sam} = 1.6E4$, corresponding to the case in Fig. 2 in this paper)

(see Eq. (9)) considering the Hamiltonian dynamic constraints on the solar angle direction. To further improve the density accuracy while still granting an improved computational efficiency, the adaptive determination of the division number and the division direction for the multi-segment method can be given into an insight in the future work. We have to mention that for a specific test case to be considered, the described four-segment division standard can only be considered a guideline for the division of the highly deformed and elongated density distribution for a highly nonlinear density propagation problem (such as the bifurcation case examined in this paper). For the specific nonlinear dynamics considered for other problems, a prior analysis on the choice of the segments is required.

3.1.3 Linear interpolation with the MAT method

With the divided four segments from MS method (presented in Sect. 3.1.2 in this paper), now we can apply the AT method (given in Sect. 3.1.1 in this paper) to each divided segment to obtain the alpha shape-based interpolated density for the highly deformed and elongated density distribution for the bifurcation case. Note that, for each segment, we need to predefine the appropriate value of the alpha radius r_{ai} for the corresponding ith segment Sg_i (i.e., we need to predefine the alpha radius vector $\boldsymbol{r}_a = \{r_{a1}, r_{a2}, r_{a3}, r_{a4}\}$ for the corresponding four segments $\{Sg_1, Sg_2, Sg_3, Sg_4\}$). This is important because the selection of the alpha radius for each segment decides how accurate the alpha shape triangulation characterises the actual shape of the density distribution.

Here we present the computation procedure for performing the multi-segment shape-based linear interpolation,

$$n_{ma}(x_1, x_2, t) = \sum_{j=1}^{N_{sg}} \sum_{i=1}^{V_{Aj}} n_{ai-j} B_{ai-j}(x_{1-j}, x_{2-j}) \qquad (10)$$

where $n_{ma}(x_1, x_2, t)$ is the multi-segment alpha shape triangulation-based linear interpolated density of the point (x_1, x_2), N_{sg} is the number of the divided segments for the MAT method (in this paper, $N_{sg} = 4$), n_{ai-j} is the value of the density for the ith vertex for the alpha shape triangulation for the jth segment Sg_j, $B_{ai-j}(x_{1-j}, x_{2-j})$ is the barycentric coordinates of the ith vertex including the point (x_{1-j}, x_{2-j}) for the alpha shape triangulation for the jth segment Sg_j.

Similarly, we can apply the MS method to the DT method to formulate the Multi-segment Delaunay Triangulation-based linear interpolation method (MDT).

To give an insight into the performance of the MAT method compared with that of the MDT method in performing the linear interpolation for the bifurcation case for the highly deformed and elongated density distribution, Fig. 6 shows the illustration and comparison for the MDT and MAT methods for the bifurcation case at time $t = 1.5$ years, where the red solid points are the $N_{sam} = 1.6E4$ propagated samples in the (ϕ, e) 2D phase space. As we can see in Fig. 6a, for the overall density distribution for the bifurcation case, for the MDT method, gray interpolated points are generated within the whole convex hull of the scattered sample data for the divided four segments (see Fig. 5b). Note that this is the improved result for the MDT method than that for the DT method (i.e., as we can infer from Fig. 6a, compared with the MDT method, for the DT method, more gray interpolated points that are outside the actual non-convex hull of the scattered sample data will be generated for the overall elongated density distribution). For the MAT method, the compact alpha shape triangulation enclosing all the samples is generated for a predefined alpha radius vector $\mathbf{r}_a = \{1, 0.03, 15, 15\}$ corresponding to the four segments $\{Sg_1, Sg_2, Sg_3, Sg_4\}$. Figure 6b gives the snapshot around the points $(\phi, e) = (-0.7850, 0.6660)$ and $(\phi, e) = (1.5620, 0.7611)$ for the MAT method. Note that the snapshot around the right point $(\phi, e) = (1.5620, 0.7611)$ shows the interpolated density where the two segments $\{Sg_2, Sg_3\}$ connect. Compared with the results around the left point $(\phi, e) = (-0.7850, 0.6660)$ within the segment Sg_1, lower continuity and sparser interpolation are shown for the snapshot around the right point $(\phi, e) = (1.5620, 0.7611)$. This is because of the intrinsic limitation of the multi-segment method given in this paper, which gives the four segment division standard considering the Hamiltonian dynamic constraints on the solar angle direction (i.e., it is not large in the segment division number and is manually divided on the solar angle direction). From Fig. 6b we can see that, for this case with a large sample number $N_{sam} = 1.6E4$, the MAT method works better for the density interpolation than the MDT method, which adapts to the actual shape of the density space volume.

3.2 B2 binning method

With the interpolated density for the four segments from the MAT method in the vectors $(x_1, x_2, n_{ma}(x_1, x_2, t))$ at time t, the B2 binning method is used in this paper for density calculation.

To calculate the joint and marginal density for the B2 method, three steps are required. First, partition the density weights $n_{ma}(x_1, x_2, t)$ into the 2D uniformly divided bins in the vectors (x_1, x_2). Second, with the defined 2D bins, calculate the joint density as the weighted sum of density weights per bin area, as follows [24],

$$f_{DEE-pk}(x_1, x_2, t) = \frac{S_{pk}/A_{pk}}{\sum_{p=1}^{B_x} \sum_{k=1}^{B_y} S_{pk}} \qquad (11)$$

where S_{pk} is the sum of the density weights $n_{ma}(x_1, x_2, t)$ in each bin, $p \in \{1, \cdots, B_x\}$, $k \in \{1, \cdots, B_y\}$, B_x and B_y are the defined bin number for the two state space directions, respectively, A_{pk} is the area for each bin. Third, calculate the marginal density for each direction by integrating the joint density throughout the whole domain of the other direction. Here we present the equation for the marginal density for the first dimension [24],

$$f_{DEE-1}(x_1, t) = \frac{A_{pk} \cdot \sum_{x_2=L_2}^{U_2} f_{DEE-pk}(x_1, x_2, t)}{wid_1}, p$$
$$= \{1, \ldots, B_x\} \qquad (12)$$

where L_2 and U_2 are the lower and upper bounds of the bin edges for the second dimension, respectively, wid_1 is the bin width for the first direction. As we can see in Eq. (12), for the B2 method, the marginal density for x_i represents the weighted sum of the density weights per bin width of wid_i, $i \in \{1,2\}$.

3.3 Density propagation with the MAT-B2 method

In this section, we first present the whole procedure for solving the bifurcation case for the long-term density propagation problem with the MAT-B2 method presented in this paper. Then the integrated illustration and comparison for the DEE methods of DT-B1, MDT-B1 and MAT-B2 is given.

Table 1 gives the computation procedure for solving the bifurcation case for the long-term density propagation problem with the MAT-B2 method. To help better understand the MAT-B2 method, Fig. 7 summarises the flowchart of the proposed MAT-B2 method for density propagation including the clear indication of the parameters and the assumptions that must be known in advance, and the inputs and outputs of each step. Table 2 shows the combinations of options for DEE methods of DT-B1, MDT-B1 and MAT-B2, in terms of the composition of the linear interpolation method and the binning method. Note that the performance of the DT-B1 method for density propagation for the bifurcation case is low in the joint and marginal density accuracy (see in Figs. 3 and 4 in Sect. 2.3 in this paper), and it will not be further studied in the following paper. Compared with the DT-B1 method, the MDT-B1 method is the combination of

the MDT method (i.e., multi-segment DT method, defined in Sect. 3.1.3 in this paper) and the B1 method for density propagation. It is given in this paper as a baseline method to demonstrate the superiority of the MAT method and the B2 method for the MAT-B2 method. Also note that to make sure of the density quality with a low computational effort, in this paper, we select the suitable sample number N_{sam} for dynamic propagation and the suitable grid number $Ngrid$ for performing the linear interpolation via the trade-off between the density accuracy and the computational efficiency.

4 Simulation setup

4.1 Definition of the initial conditions for the MEO planar phase space case

To improve the density accuracy for the bifurcation case for the long-term density propagation problem (see Figs. 2, 3, 4) within the continuum method framework, we will focus on the bifurcation case given in Sects. 2.1 and 2.3 in this paper, and focus on improving the density accuracy for the case at time $t = 1.5$ yrs when passing through the bifurcation point P_4 (see Fig. 2). Table 3 rewrites the initial conditions for the bifurcation case in terms of the mean $\boldsymbol{m}_0$ and the covariance matrix $\boldsymbol{P}_0$ of the initial Gaussian density distribution and the propagation time t. It should be reminded that, here the initial conditions for the Gaussian samples are specified to make sure of the realisation of the long-term density propagation within

Table 1 Computation procedure for solving the bifurcation case for the long-term density propagation problem with the MAT-B2 method

| Step	Content
1	Determine initial conditions:
	1) Formulate the dynamics for the phase space and the density evolution (Eqs. (1), (5));
	2) Give the mean $\boldsymbol{m}_0$ and the covariance matrix $\boldsymbol{P}_0$ for the initial Gaussian distribution, and the density propagation time t;
	3) Select a predefined alpha radius r_{ai} for the ith segment Sg_i (divided via the four-segment division standard (Eq. (9))), for generating a compact alpha shape triangulation enclosing all the samples;
2	Select the sample number N_{sam} and the grid number $Ngrid$ by trading off the accuracy and efficiency;
3	Conduct improved multi-segment alpha shape triangulation-based linear interpolation for propagated samples (Eq. (10));
4	Conduct the B2 binning method for the interpolated density for density calculation (Eqs. (11), (12));
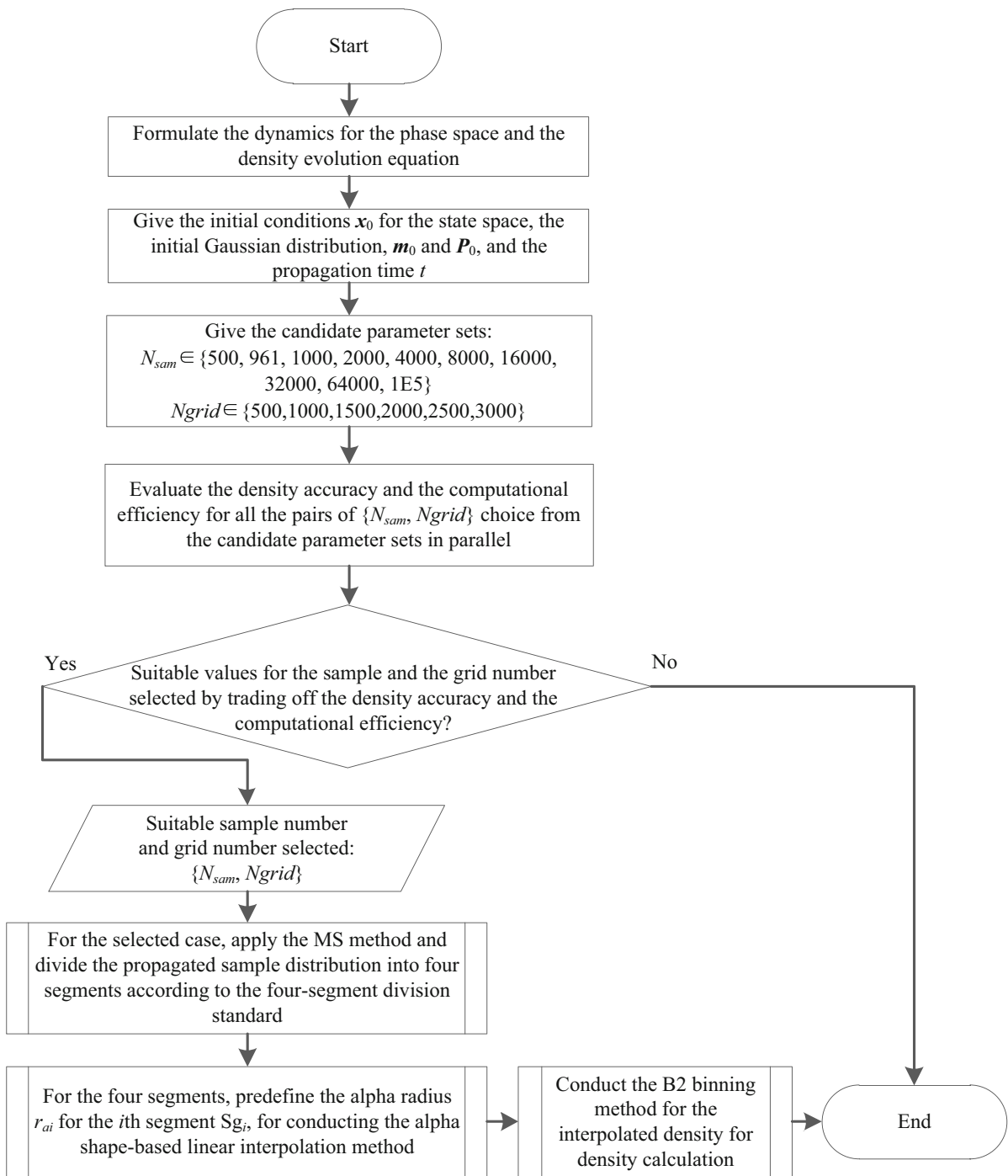
Fig. 7 Flowchart of the proposed MAT-B2 method for density propagation

two sub-phase space domains {SubD$_3$, SubD$_2$} that include the bifurcation point P$_4$ (see Figs. 1b and 2a).

To complement the accuracy and efficiency analysis for the MAT-B2 and MDT-B1 methods, a MC

simulation is done for the test case in Table 3. The number of the MC samples is set to be N_{sam} = 1E5 for ensuring the convergence of the MC method and

Table 2 Illustration and comparison for the composition of DEE methods

DEE method	DT-B1	MDT-B1	MAT-B2
Linear interpolation method	DT	MDT	MAT
Binning method	B1	B1	B2

avoiding a higher computational load for a test case with a larger sample number.

To give a better choice of the sample number N_{sam} and the grid number $Ngrid$ for the DEE methods, the sample number N_{sam} is chosen within the parameter set, $N_{sam} \in \{500, 961, 1000, 2000, 4000, 8000, 16,000, 32,000, 64,000, 1E5\}$, and the grid number is chosen within the parameter set, $Ngrid \in \{500, 1000, 1500, 2000, 2500, 3000\}$. Table 4 summarises the predefined parameter sets of N_{sam} and $Ngrid$. The two parameter sets are defined in this paper for the following considerations. For the parameter set of the sample number N_{sam}, it is set to be exponentially distributed except the two elements $\{961, 1E5\}$, which are the reference sample number for the cases of DEE-961 and DEE-1E5 in the work of [22]. In [22], we can see that, for the case with more samples (i.e., DEE-1E5), the high density accuracy level comparable with that of the MC method can be achieved, but at the cost of a high computational effort. For the case with fewer samples (i.e., DEE-961), when the phase space is highly deformed and elongated, the density accuracy level is low. Thus, within the parameter domain [500, 1E5], the evolution characteristic for the density accuracy and the computational efficiency with respect to the N_{sam} can be preliminarily exploited, for the bifurcation case for the highly deformed and

elongated density distribution. For the parameter set of the grid number $Ngrid$, it is set to be linearly distributed. As we can infer in [22], only when the number of the propagated samples N_{sam} is large enough for capturing the deformed and elongated density distribution, accurate density can be calculated via the linear interpolation and the binning methods. Thus, for the contribution of the density accuracy and the computational efficiency, the value of the sample number N_{sam} may weigh much more than the grid number $Ngrid$ in affecting the accuracy and the efficiency for the DEE method. Within the domain [500, 3000], the evolution characteristic for the density accuracy and the computational efficiency with respect to the $Ngrid$ can be preliminarily exploited.

4.2 Definition of the accuracy measure

To determine the density accuracy for DEE methods with respect to that of MC, in this paper, the Likelihood Deviation (LD) is used as the accuracy measure as follows [23]

$$LD = \frac{\sqrt{\sum_{j=1}^{N} \left(f_{\text{DEE}}(\mathbf{x}_j) - q(\mathbf{x}_j) \right)^2}}{N} \tag{13}$$

where N is the number of MC samples, $\mathbf{x}_j$ is the jth MC sample, $f_{\text{DEE}}(\mathbf{x}_j)$ is the density of the jth MC sample for the DEE methods, $q(\mathbf{x}_j)$ is the density of the jth MC sample for the MC method. The LD measure quantifies the density accuracy for the DEE methods compared with that of the MC method. The smaller the LD measure, the higher density accuracy for the DEE methods compared with that of the MC method.

Table 3 Initial conditions (the initial Gaussian distribution and the propagation time) for the bifurcation case

Variable	mean, $\mathbf{m}_0$ [rad; -]	Covariance matrix, $\mathbf{P}_0$	t, [yr]
Value	$[\, e_0, \phi_0] = [\, 0.245, 0.4495]$	diag$\{6.25E-4, 0.0096\}$	1.5

Table 4 Predefined parameter sets of the sample number N_{sam} and the grid number $Ngrid$ for DEE methods

Variable	N_{sam}	$Ngrid$
Predefined parameter set	$\{500, 961, 1000, 2000, 4000, 8000, 16,000, 32,000, 64,000, 1E5\}$	$\{500, 1000, 1500, 2000, 2500, 3000\}$

For the case in examination, to evaluate the overall accuracy level for DEE methods with respect to that of the MC method, the following performance index J_p is predefined as the weighted sum of the LD measure for the joint and marginal density,

$$J_p = w_d \cdot \sum \text{LD} \qquad (14)$$

where w_d is the density weight, $\sum$LD is the sum of the LD measure for the joint and marginal density. In this paper, we assume the same weight $w_d = 1/3$ for the joint and marginal density for the 2D problem. The smaller the performance index J_p, the higher overall accuracy level for the DEE method compared with that of the MC method.

5 Results and discussion

It should be noted that the novelty of this paper is to study the bifurcation case for the long-term density propagation problem, and to improve the density accuracy for the bifurcation case for the highly deformed and elongated density distribution using the improved MAT-B2 method. In this paper, the MEO planar phase space case is chosen (see Sects. 2.1 and 4) to give an insight into the bifurcation case for the long-term density propagation problem in the context of high-altitude and high area-to-mass ratio satellite long-term propagation [14, 22, 23, 26].

In this section, the results are given for the bifurcation case at time $t = 1.5$ yrs (presented in Table 3) in the three sections as follows. Section 5.1 gives the selected sample number N_{sam} and the grid number $Ngrid$ by trading off the density accuracy and the computational efficiency. Section 5.2 presents the results for the MAT-B2, MDT-B1 methods. In Sect. 5.3, some discussion is given on the superiority of the MAT-B2 method for solving the bifurcation case for the long-term density propagation problem in terms of the density accuracy and the computational efficiency.

5.1 Selection of the sample number N_{sam} and grid number $Ngrid$ (for the bifurcation case, at $t = 1.5$ years)

To select the better value of the sample number and the grid number for the MAT-B2 method, we perform the accuracy and the efficiency analysis for the predefined parameter sets of the sample number N_{sam} and the grid number $Ngrid$ (see Table 4). The density accuracy is evaluated via the LD measure and the performance index J_p (see Eqs. (13), (14)). The computational efficiency is evaluated via the normalised computational effort with respect to that of the MC method.

For the bifurcation case at time $t = 1.5$ yrs, the values of the sample number and the grid number are selected as $N_{sam} = 1.6E4$, $Ngrid = 1000$ for the MAT-B2 method. Figure 8 presents the evolution of the normalised LD measure for the joint and marginal density with N_{sam}, and with $Ngrid$, respectively, for the MAT-B2 and MDT-B1 methods with respect to the case MAT-B2 ($N_{sam} = 1.6E4$, $Ngrid = 1000$). Note that the smaller the normalised LD measure for a specific $N_{sam}/Ngrid$ case, the higher accuracy level for the specific case with respect to the selected case MAT-B2 ($N_{sam} = 1.6E4$, $Ngrid = 1000$). For the case in examination, to perform the accuracy analysis for the DEE methods (via the LD measure and the predefined performance index), B_x and B_y are given as the bin numbers for the solar angle and the eccentricity directions, respectively, for the joint density calculation, for the MAT-B2 and MDT-B1 methods. The grid number $Ngrid$ gives the bin number for two phase space directions for performing the linear interpolation for all the DEE methods and represents the bin number for the two phase space directions for the marginal density calculation. Figure 9 shows the evolution of the normalised performance index with N_{sam} and with $Ngrid$, respectively, with respect to the case MAT-B2 ($N_{sam} = 1.6E4$, $Ngrid = 1000$). Also in this case, the smaller the normalised performance index, the higher overall accuracy level for the specific case with respect to the selected case MAT-B2 ($N_{sam} = 1.6E4$, $Ngrid = 1000$). Figure 10 presents the evolution of the normalised computational effort with N_{sam}, and with $Ngrid$, respectively, with respect to that of the MC method.

Here we present the procedures for determining the sample number $N_{sam} = 1.6E4$ for the MAT-B2 method by trading off the density accuracy and the computational efficiency. First, as we can see in Fig. 8a, for the sample number $N_{sam} \leq 1.6E4$, the smallest LD measure (i.e., the highest density accuracy) for the joint density and the marginal density in both phase space directions is obtained for the MAT-B2 method. For the sample number $N_{sam} > 1.6E4$, the slightly larger LD measure for the marginal density in both

Fig. 8 Normalised LD evolution **a** with N_{sam}, and **b** with $Ngrid$, for DEE methods, with respect to the case MAT-B2 ($N_{sam} = 16{,}000$, $Ngrid = 1000$), for the bifurcation case, at time $t = 1.5$ years
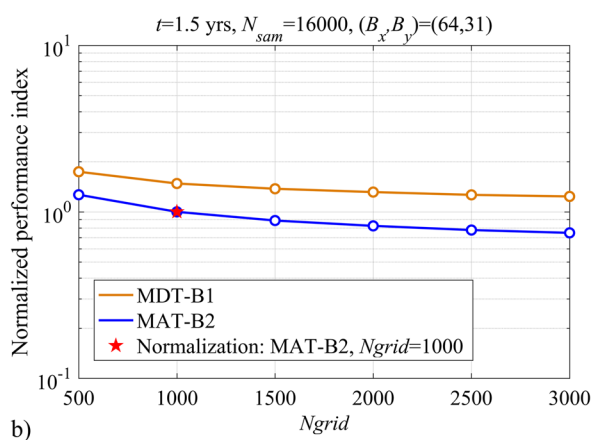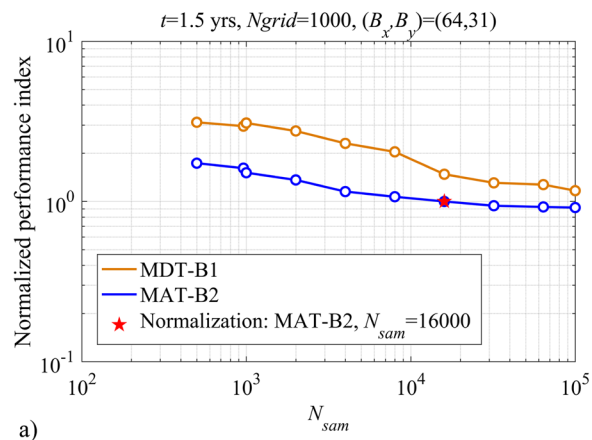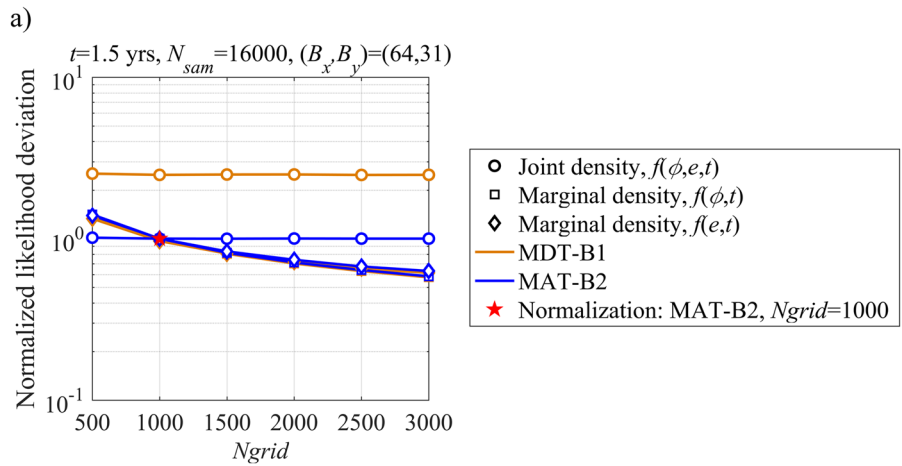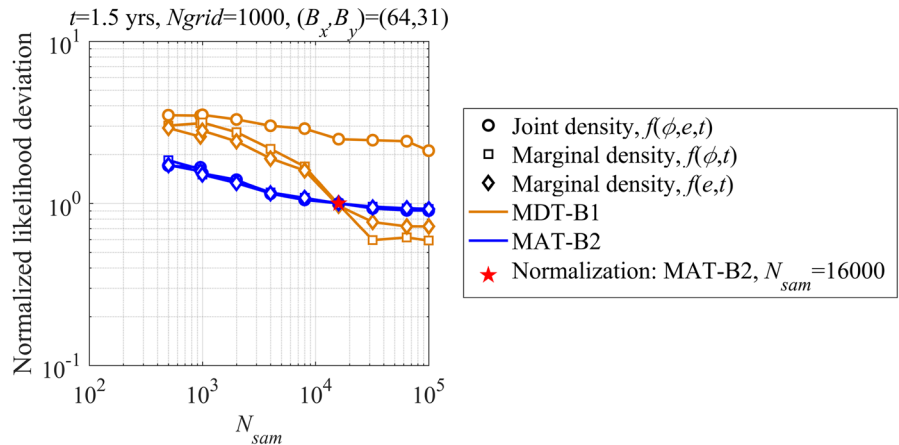

a)

b)

a)

b)

Fig. 9 Normalised performance index J_p evolution **a** with N_{sam}, and **b** with $Ngrid$, for DEE methods, with respect to the case MAT-B2 ($N_{sam} = 16{,}000$, $Ngrid = 1000$), for the bifurcation case, at time $t = 1.5$ years

phase space directions is got for the MAT-B2 method, but little discrepancy is shown for the MAT-B2 and MDT-B1 methods (indicating the comparable high

accuracy level for the two methods). Overall, for the MAT-B2 and MDT-B1 methods, the LD measure for the joint and marginal density drops consistently with
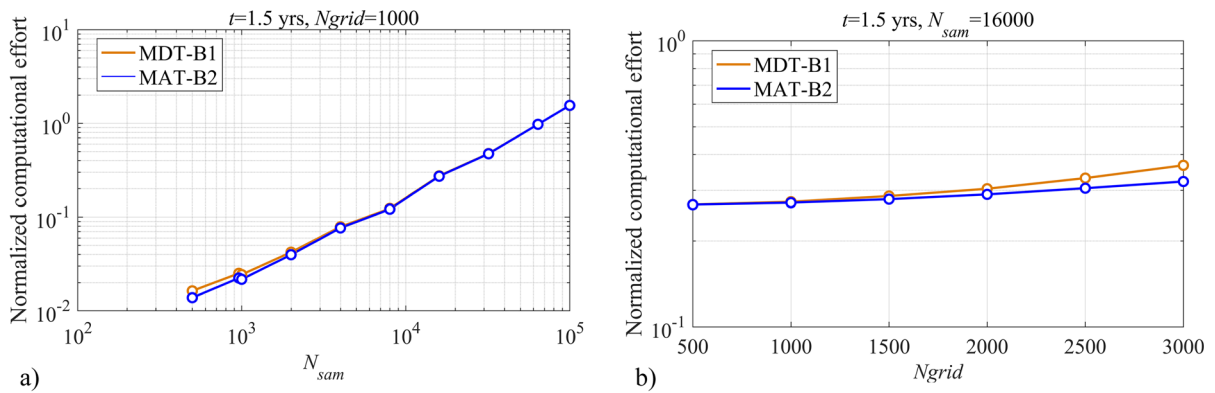
Fig. 10 Normalised computational effort evolution **a** with N_{sam}, and **b** with $Ngrid$, for DEE methods, with respect to the MC method, for the bifurcation case, at time $t = 1.5$ yrs

the increase of the sample number N_{sam}, indicating the high density accuracy stability with respect to the sample number. Second, as we can see in Fig. 9a, the smaller performance index J_p is obtained for the MAT-B2 method than that for the MDT-B1 method. The overall method accuracy ranking MAT-B2>MDT-B1 is obtained. This is as expected, because for the MAT-B2 method, the linear interpolation is done within the compact non-convex hull enclosing all the samples for the four divided segments (see Fig. 6b). This neglects many Delaunay triangulation-based interpolated points outside the alpha shape triangulation. In this case, the weights for the interpolated points within the alpha shape triangulation for the multiple segments for the MAT method are increased compared with that for the MDT method. The higher accuracy is achieved in capturing the core values, and the distribution characteristics of the joint and marginal density. Also note that, for the MAT-B2 method, the joint density is calculated as the weighted sum of the density weights per bin area, which allows for the variant nonlinearity of the density within each alpha shape triangulation. For the sample number N_{sam}>1.6E4, little changing amplitude is shown for the evolution of the performance index for the MAT-B2 method, indicating the high stability for the overall density accuracy level ranking. Third, from Fig. 10a, we can see that the normalised computational effort evolves exponentially with the sample number N_{sam} for MAT-B2 and MDT-B1 methods. Note that here in Fig. 10, the coordinates for the two phase space directions are plotted using a log scale. The method efficiency ranking MAT-B2>MDT-B1 is obtained.

Overall, little discrepancy is shown for the normalised computational effort for MAT-B2 and MDT-B1 methods. This is because the main difference between the MAT-B2 and MDT-B1 methods is the post-processing for the propagated samples using the different linear interpolation and binning methods (see Table 2). For the MAT-B2 method, less interpolated points (within the compact alpha shape triangulation for the four segments) are processed than that for the MDT-B1 method (within the whole convex hull for the four segments) for density calculation (see Fig. 6). With the increase of the sample number, i.e., for $N_{sam} \geq 4000$, the computational effort part of the dynamic propagation of the samples makes up the main part of the total computational effort, compared with the computational effort part of the density calculation using the linear interpolation and the binning methods. This leads to the overall little difference for the normalised computational effort for the MAT-B2 and MDT-B1 methods. For the bifurcation case at time $t = 1.5$ yrs, the computation time for the MC method is 384.65 s. For the MAT-B2 method, for the case $N_{sam} = 1.6E4$, the computational effort accounts for 27.16% of that of the MC method. From Fig. 10a, we can infer that, for the MAT-B2 method, for a case with the sample number $N_{sam} \leq 3.38E4$, the computational effort can be ensured to be under 50% of that of the MC method. Basing on the above three-aspect analysis, we select the sample number $N_{sam} = 1.6E4$ for the MAT-B2 method for the bifurcation case, with the highly accurate density and the high computational efficiency.

Through a similar procedure, as we can see in Figs. 8b, 9b and 10b, the better value of the grid number *Ngrid* = 1000 is selected for the MAT-B2 method.

For the MAT-B2 method, as we can see in Figs. 8, 9 and 10, for the normalised LD measure for the joint and marginal density, the normalised performance index, and the normalised computational effort, larger changing amplitudes are shown with respect to the sample number than the grid number. This indicates the higher influence of the sample number than the grid number in affecting the density accuracy and the computational efficiency. This is not unexpected, because only when the sample number is large enough for characterising the highly nonlinear density distribution, accurate density can be calculated using the linear interpolation and the binning methods for a selected grid number. For MAT-B2 and MDT-B1 methods, no apparent change is shown for the evolution of the LD measure for the joint density with the grid number, while the LD measure for the marginal density drops consistently with the increase of the grid number (see Fig. 8b). This indicates that the selection of the grid number mainly affects the accuracy of the marginal density, not the joint density. This is because, in this paper, the marginal density is calculated and presented based on the bins used for linear interpolation. Overall, we can conclude that the MAT-B2 method outperforms the MDT-B1 method for the long-term density propagation problem for the bifurcation case in terms of the density accuracy and the computational efficiency.

To give an insight into other candidate choices of the sample number and the grid number, for solving the bifurcation case for the long-term density propagation problem, Fig. 11 shows the normalised performance index J_p (Fig. 11a), the normalised LD measure for the joint density (Fig. 11b), the normalised LD measure for the marginal density of the solar angle (Fig. 11c), the normalised LD measure for the marginal density of the eccentricity (Fig. 11d), for the MAT-B2 method, in the *Ngrid-N_sam* 2D space. Note that results in Fig. 11 are normalised with respect to the case MAT-B2 (N_{sam} = 1.6E4, *Ngrid* = 1000). Figure 12 shows the normalised computational effort in the *Ngrid-N_sam* 2D space for the MAT-B2 method, normalised with respect to that of the MC method. As we can see in Fig. 11, overall, the sample number N_{sam} plays a more important role than the grid number

Ngrid in affecting the density accuracy, which is especially the case for the joint density (see Fig. 11b). This is consistent with what we have concluded from Figs. 8, 9 and 10. Also, from Fig. 12, we can see that the sample number plays a more important role than the grid number in affecting the computational load. For the DEE methods, the main computational effort is the dynamic propagation part for propagating the N_{sam} samples.

5.2 Density results (for the bifurcation case, at *t* = 1.5 years)

With the selected sample number and grid number {N_{sam} = 1.6E4, *Ngrid* = 1000} for the bifurcation case at time *t* = 1.5 yrs, now we present the joint and marginal density in Figs. 13 and 14, for the MAT-B2 method compared with the MDT-B1 method with respect to that of the MC method. To highlight the higher density accuracy stability for the MAT-B2 method than the MDT-B1 method with the increase of the sample number N_{sam} (see Figs. 8a, 9a), in Figs. 13 and 14, we present also the density for a larger sample number case with {N_{sam} = 1E5, *Ngrid* = 1000}, which has the same sample number N_{sam} = 1E5 as that of the MC method.

From Figs. 13a and 14 for the MC method (in gray), we can see that, for the bifurcation case at time *t* = 1.5 yrs for the highly deformed and elongated density distribution, high nonlinearity is shown in the joint density and the marginal density in two phase space directions. This is especially the case for the marginal density. For the marginal density for the solar angle (see Fig. 14a for the MC method), a peak value is detected at $\phi = -0.2962$ (marginal density value: 4.952; unit of the marginal density of the solar angle for the MC method: frequency of samples per bin width in the solar angle direction). High nonlinearity (or steepness) is shown within the solar angle domains $[-0.3777, -0.2962]$ and $[-0.2962, 1.152]$. For the marginal density for the eccentricity, two local marginal density peaks are detected at $e = 0.3725$ and $e = 0.8118$. The marginal density values for the two density peaks are 4.422 and 3.308 (unit of the marginal density of the eccentricity for the MC method: frequency of samples per bin width in the eccentricity direction). Note that, due to the highly nonlinear distribution characteristic for the marginal density of the eccentricity, a local minimum density
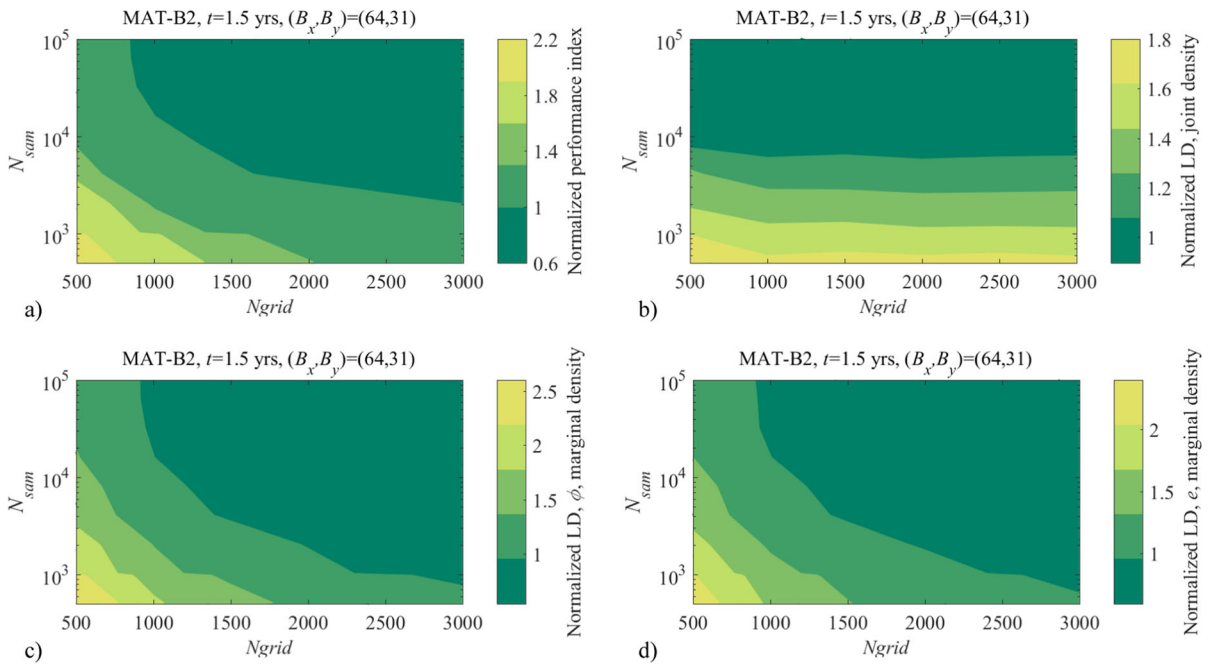
a)

b)

c)

d)

Fig. 11 **a** Normalised performance index J_p, **b** normalised LD measure for the joint density, **c** normalised LD measure for the marginal density of the solar angle, **d** normalised LD measure for the marginal density of the eccentricity, in the $Ngrid$-N_{sam} 2D space (normalised with respect to the case MAT-B2 ($N_{sam} = 16,000$, $Ngrid = 1000$)), for the MAT-B2 method for the bifurcation case, at time $t = 1.5$ yrs
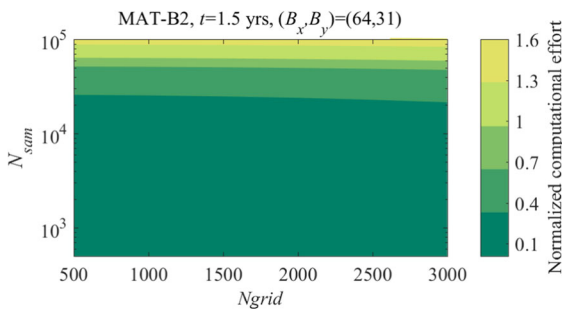

Fig. 12 Normalised computational effort, in the $Ngrid$-N_{sam} 2D space, for the MAT-B2 method (normalised with respect to that of the MC method, for the bifurcation case, at time $t = 1.5$ yrs

value is detected at $e = 0.7654$ (marginal density value: 0.266). High nonlinearity is shown within the eccentricity domain [0.3725, 0.8118] between the two local density peaks (see Fig. 14c for the MC method) (i.e., when decreasing from the larger local density peak at $e = 0.3725$, till the local density trough at $e = 0.7654$, and then increasing to the smaller local density peak at $e = 0.8118$). Overall, high nonlinearity is shown for the marginal density in two phase space directions in terms of the multiple local density peaks (for the marginal density of the eccentricity), and the

local density trough between the two local density peaks (for the marginal density of the eccentricity), and the high nonlinearity (or steepness) shown in the overall density evolution characteristics. This is consistent with the high dynamic nonlinearity for the bifurcation case for the planar phase space after long-term propagations (see Fig. 5a) when approaching the eccentricity domain larger than the critical eccentricity ($e_{cri} = 0.6$) or approaching the zero eccentricity, (or approaching the solar angle $\phi = 0$ or $\phi = 1/2\pi$).

As shown in Figs. 13a and 14, for the selected cases with $\{N_{sam} = 1.6E4, Ngrid = 1000\}$, the higher accuracy in the joint density with respect to that of the MC method (see Fig. 13a) is obtained for the MAT-B2 method (see Fig. 13d) than the MDT-B1 method (see Fig. 13b). With the increase of the sample number N_{sam}, little discrepancy is shown in the joint density accuracy for the MAT-B2 method than the MDT-B1 method (for the MAT-B2 method, see Figs. 13d, e; for the MDT-B1 method, see Fig. 13b, c). This indicates the higher accuracy stability for the joint density with respect to the sample number N_{sam} for the MAT-B2 method. This is consistent with the aforementioned results in Figs. 8a and 9a.
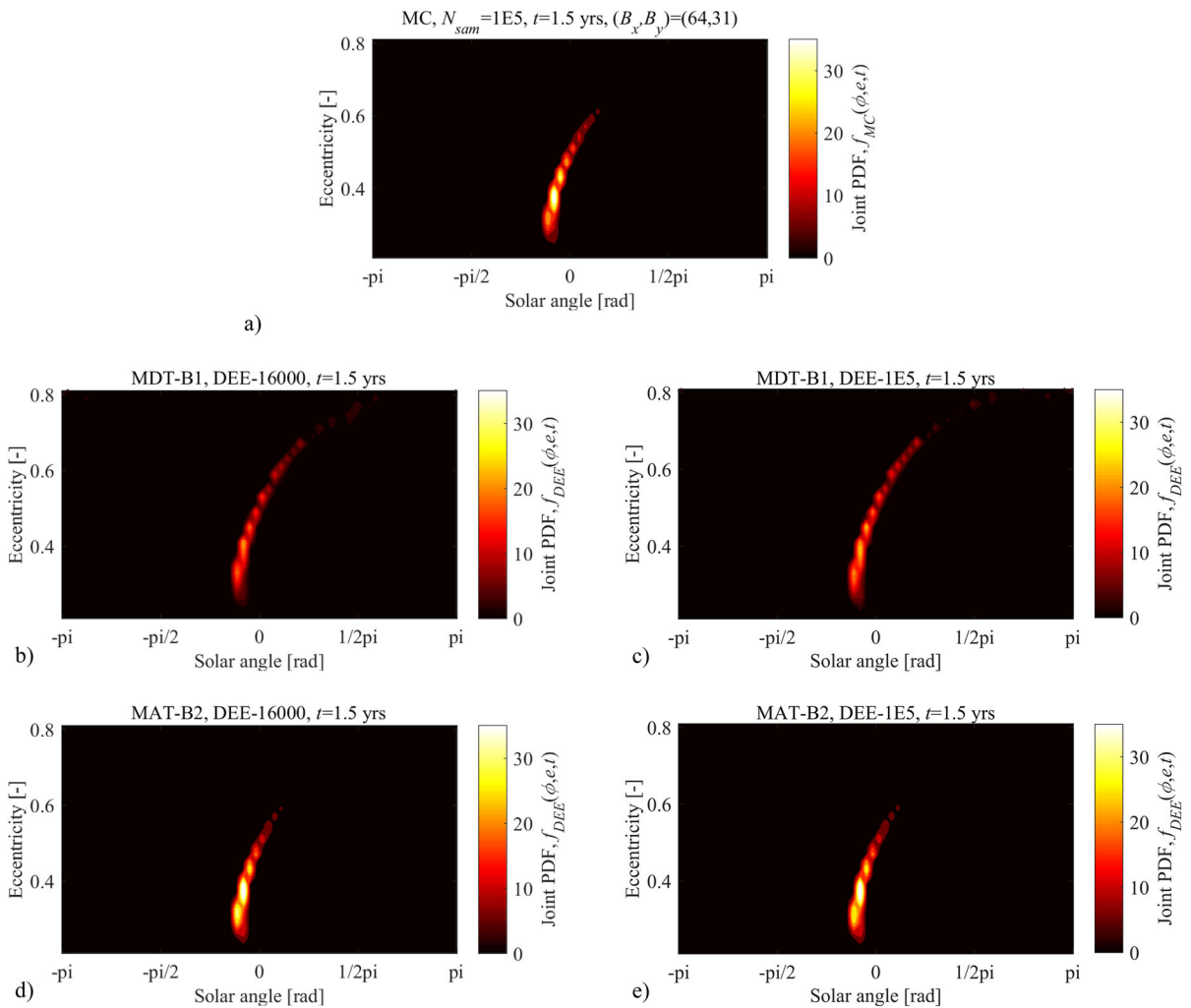
Fig. 13 The joint density **a** for the MC method; for the MDT-B1 method, with **b** {N_{sam} = 1.6E4, $Ngrid$ = 1000}, **c** {N_{sam} = 1E5, $Ngrid$ = 1000}; for the MAT-B2 method, with **d** {N_{sam} = 1.6E4, $Ngrid$ = 1000}, **e** {N_{sam} = 1E5, $Ngrid$ = 1000}; for the bifurcation case, at time t = 1.5 years

Similarly, for the marginal density of the solar angle (see Fig. 14a, b), for the selected cases with {N_{sam} = 1.6E4, $Ngrid$ = 1000}, the higher accuracy is obtained for the MAT-B2 method (in blue) than the MDT-B1 method (in yellow) with respect to that of the MC method (in gray). For the MDT-B1 method, the marginal density of the solar angle is overestimated within the solar angle domain [0.4561, 1.516]. This is because for the MDT-B1 method, the overinterpolated density is got within the whole convex hull for the segment Sg_2 (see Fig. 6a). For the MAT-B2 method, the inclusion of the alpha shape helps capture the actual non-convex shape of the density distribution (see Fig. 6b). For the marginal density of the

eccentricity (see Fig. 14c, d), for the selected cases with {N_{sam} = 1.6E4, $Ngrid$ = 1000}, the MAT-B2 method outperforms the MDT-B1 method in capturing the overall density distribution characteristics, including the two local density peaks at e = 0.3725 and e = 0.8118, and the overall highly nonlinear density evolution characteristics from the eccentricity e = 0.3725 (the larger local density peak), to e = 0.7654 (the local density trough), and to e = 0.8119 (the smaller local density peak), highly consistent with that of the MC method. For the MDT-B1 method, it underestimates the density peak values at e = 0.3725 and e = 0.8118, and works badly in capturing the highly nonlinear density evolution
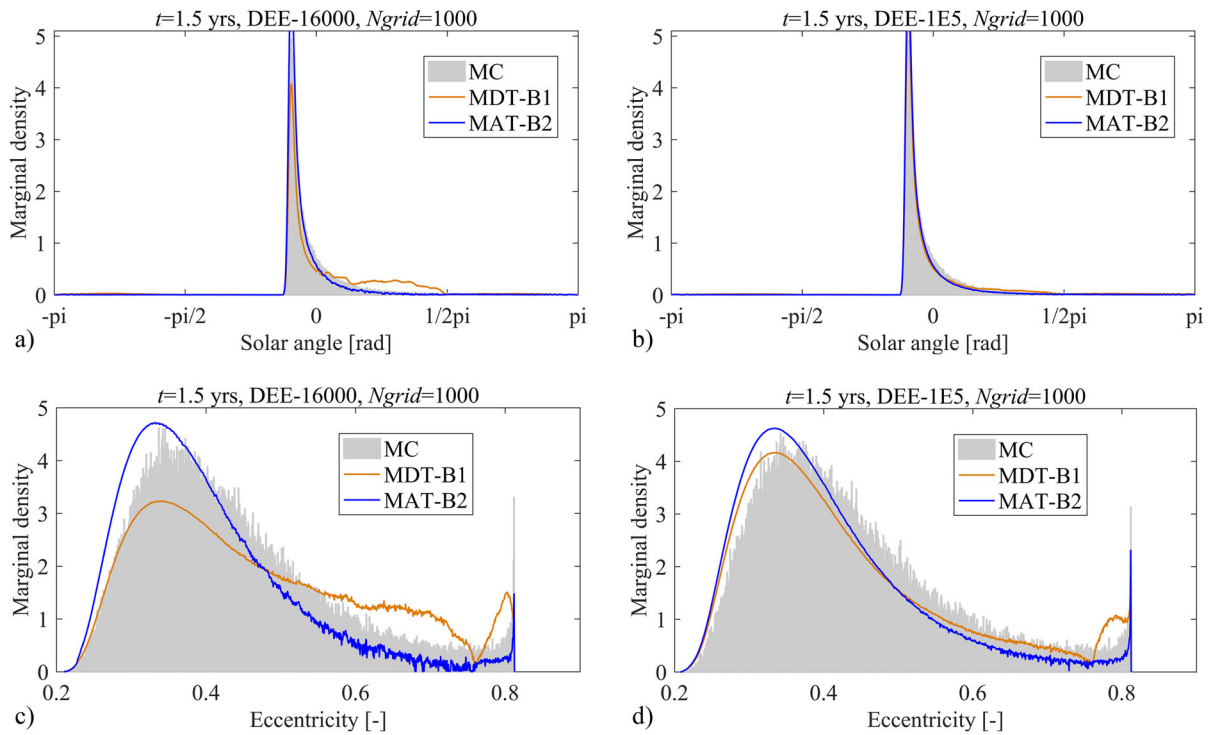
Fig. 14 The marginal density of the solar angle with **a** {N_{sam} = 1.6E4, $Ngrid$ = 1000}, **b** {N_{sam} = 1E5, $Ngrid$ = 1000}, and the marginal density of the eccentricity with **c** {N_{sam} = 1.6E4, $Ngrid$ = 1000}, **d** {N_{sam} = 1E5, $Ngrid$ = 1000}, for MDT-B1, MAT-B2 methods with respect to the MC method, for the bifurcation case, at time t = 1.5 years

characteristics between the two local density peaks; also, within the eccentricity domain [0.7599, 0.8107], the marginal density of the eccentricity is overestimated due to the overinterpolation within the whole convex hull of the two segments Sg_3 and Sg_4 (see Fig. 6a). With the increase of the sample number with N_{sam}, less discrepancy is shown in the marginal density of the solar angle and the eccentricity for the MAT-B2 method than the MDT-B1 method. This indicates the higher accuracy stability for the marginal density with respect to the sample number N_{sam} for the MAT-B2 method. It should be noted that, for the MAT-B2 method, within the eccentricity domain [0, 0.3725], the marginal density of the eccentricity is slighted overestimated, and within the eccentricity domain [0.4964, 0.8118], it is slighted underestimated. This is due to the intrinsic numerical nature for the MAT-B2 method within the continuum method framework, which calculates the joint and marginal density as the weighted sum of the density weights per bin area and per bin width, respectively (i.e., in a statistical way similar to that of the MC method).

Meanwhile, for the multi-segment method introduced in this paper, the determination of the alpha radius vector r_a affects the interpolation accuracy for the four divided segments, which further affects the accuracy for the B2 method for density calculation. Overall, from Figs. 10, 13 and 14, we can conclude that for the bifurcation case for the highly deformed and elongated density distribution, for the selected case {N_{sam} = 1.6E4, $Ngrid$ = 1000}, the improved accuracy in the joint and marginal density is got for the MAT-B2 method compared with that of the MDT-B1 method with respect to that of the MC method, together with the high computational efficiency compared with that of the MC method. Also note that, in this paper, the alpha radius value for each segment is manually predetermined using the dichotomy, and the four-segment division standard (see Eq. (9)) is predetermined for the multi-segment method considering the Hamiltonian constraints on the solar angle domain. To further improve the density accuracy while still granting an improved computational efficiency within the continuum method framework, the adaptive

determination of the suitable value of the alpha radius for each segment, and the adaptive determination of the division number and the division direction for the multi-segment method need to be given into an insight in the future work.

5.3 Discussion

For the bifurcation case for the highly deformed and elongated density distribution (at time $t = 1.5$ yrs, see Fig. 5), for the selected case with $\{N_{sam} = 1.6E4, Ngrid = 1000\}$, the improved accuracy in terms of the joint and marginal density is obtained for the MAT-B2 method compared with the MDT-B1 method with respect to that of the MC method (see Figs. 13 and 14). Overall, the MAT-B2 method outperforms the MDT-B1 method in capturing the core value of the joint density, the high nonlinearity for the marginal density in two phase space directions, including the multiple local density peaks and the local density trough between the two local density peaks for the marginal density of the eccentricity, and the high nonlinearity (or steepness) shown in the overall density evolution characteristics.

The advantages of the MAT-B2 method are shown in the higher density accuracy (see Figs. 13 and 14), the higher density accuracy stability with respect to the sample number N_{sam} and the grid number $Ngrid$ (see Fig. 9a and b), and the higher computational efficiency compared with that of the MC method (i.e., for the case with $\{N_{sam} = 1.6E4, Ngrid = 1000\}$, the computational effort accounts for 27.16% of that of the MC method; see Fig. 10). The sample number weighs more than the grid number in affecting the density accuracy and the computational efficiency for the DEE methods (see Figs. 8, 9 and 10). For the bifurcation case for the highly deformed and elongated density distribution, the inclusion of MS method (see Sect. 3.1.2 in this paper) for the AT method (see Sect. 3.1.1) is necessary for the accurate and efficient density propagation for the planar phase space long-term density propagation problem.

6 Conclusion

This paper studies the bifurcation case for the planar phase space long-term density propagation problem, and improves the density accuracy for the bifurcation

case for the highly deformed and elongated density distribution using an improved multi-segment alpha shape-based linear interpolation method. The improved multi-segment alpha shape-based linear interpolation method is the combination of the multi-segment method and the alpha shape triangulation-based linear interpolation method. To improve the interpolation accuracy for the bifurcation case for the overall density distribution with high deformation and elongation that extends within the whole state space domain, the multi-segment method is introduced to the alpha shape-based linear interpolation method by dividing the overall density distribution into multiple segments. A four-segment division standard considering the Hamiltonian dynamic constraints on the solar angle domain is presented to divide the overall density distribution into four segments. The suitable values of the sample number for dynamic propagation, and the grid number for performing the linear interpolation, are selected by trading off the density accuracy and the computational efficiency. For the bifurcation case for the planar phase space long-term density propagation problem in the context of high altitude and high area-to-mass ratio satellite long-term density propagation, the superiority of the MAT-B2 method in terms of the density accuracy and the computational efficiency is demonstrated compared with the MDT-B1 method with respect to that of the MC method.

Declarations

Conflict of interest The authors declare that they have no known competing financial interests or personal relationships that could have appeared to influence the work reported in this paper.

References

1. Colombo, C., McInnes, C.R.: Evolution of Swarms of 'Smart Dust' Spacecraft. New Trends in Astrodynamics and Applications VI, New York (2011)
2. Evans, L. C.: Partial Differential Equations. Graduate studies in mathematics, 19(2) (1998)

3. Edelsbrunner, H., Mücke, E.P.: Three-dimensional alpha shapes. ACM Trans. Graph. **13**(1), 43–72 (1994). https://doi.org/10.1145/174462.156635

4. Feng, J., Santeramo, D., Di Lizia, P., Armellin, R., Hou, X.: Dynamical structure of the motion around asteroids with uncertain gravity and solar radiation pressure. Acta Astronaut. **186**, 135–147 (2021). https://doi.org/10.1016/j.actaastro.2021.05.023

5. Frey, S.: Evolution and hazard analysis of orbital fragmentation continua. Doctoral thesis. Politecnico di Milano. Supervisors: Colombo, C., Lemmens, S., Krag, H. pp. 31–32 (2020)

6. Giza, D., Singla, P., Jah, M.: An approach for nonlinear uncertainty propagation: application to orbital mechanics. In: AIAA Guidance, Navigation, and Control Conference, AIAA Paper, pp. 2009–6082. (2009). https://doi.org/10.2514/6.2009-6082

7. Gkolias, I., Alessi, E.M., Colombo, C.: Dynamical taxonomy of the coupled solar radiation pressure and oblateness problem and analytical deorbiting configurations. Celest. Mech. Dyn. Astron. **132**(11), 1–18 (2020). https://doi.org/10.1007/s10569-020-09992-2

8. Gor'kavyi, N.N., Ozernoy, L.M., Mather, J.C.: A new approach to dynamic evolution of interplanetary dust. Astrophys. J. **474**(1), 496–502 (1997). https://doi.org/10.1086/303440

9. Gor'kavyi, N.N., Ozernoy, L.M., Mather, J.C., Taidakova, T.: Quasi-stationary states of dust flows under Poynting-Robertson drag: new analytical and numerical solutions. Astrophys. J. **488**(1), 268–276 (1997). https://doi.org/10.1086/304702

10. Halder, A., Bhattacharya, R.: Dispersion analysis in hypersonic flight during planetary entry using stochastic Liouville equation. J. Guid. Control. Dyn. **34**(2), 459–476 (2016). https://doi.org/10.2514/1.51196

11. Hamilton, D.P.: Erratum: motion of dust in a planetary magnetosphere: Orbit-averaged equations for oblateness, electromagnetic, and radiation forces with application to Saturn's e-ring. Icarus **103**, 161 (1993). https://doi.org/10.1006/icar.1993.1065

12. Hamilton, D.P., Krivov, A.V.: Circumplanetary dust dynamics: effects of solar gravity, radiation pressure, planetary oblateness, and electromagnetism. Icarus **123**(2), 503–523 (1996). https://doi.org/10.1006/icar.1996.0175

13. Jia, B., Xin, M.: Short-arc orbital uncertainty propagation with arbitrary polynomial chaos and admissible region. J. Guid. Control. Dyn. **43**(4), 715–728 (2020). https://doi.org/10.2514/1.g004548

14. Krivov, A.V., Getino, J.: Orbital evolution of high-altitude balloon satellites. Astron. Astrophys. **318**, 308–314 (1997)

15. Letizia, F., Colombo, C., Lewis, H.G.: Analytical model for the propagation of small-debris-object clouds after fragmentations. J. Guid. Control. Dyn. **38**(8), 1478–1491 (2015). https://doi.org/10.2514/1.G000695

16. Letizia, F., Colombo, C., Lewis, H.G.: Multidimensional extension of the continuity equation method for debris clouds evolution. Adv. Space Res. **57**(8), 1624–1640 (2016). https://doi.org/10.1016/j.asr.2015.11.035

17. Letizia, F., Colombo, C., Van den Eynde, J., Armellin, R., Jehn, R.: SNAPPSHOT: Suite for the numerical analysis of planetary protection. In: the 6th International Conference on Astrodynamics Tools and Techniques (ICATT). pp. 14–17. (2016b)

18. McInnes, C.R.: Simple analytic model of the long-term evolution of nanosatellite constellations. J. Guid. Control. Dyn. **23**(2), 332–338 (2000). https://doi.org/10.2514/2.4527

19. Nazarenko, A.: The development of the statistical theory of a satellite ensemble motion and its application to space debris modeling. In: The Proceedings of the 2nd European Conference on Space Debris, ESOC. ESA SP-393 (1997)

20. Preparata, F.P., Shamos, M.I.: Computational Geometry, pp. 191–218. Springer-Verlag, New York (1985)

21. Smirnov, N.N., Nazarenko, A.I., Kiselev, A.B.: Modelling of the space debris evolution based on continua mechanics. In: the Proceedings of the 3rd European Conference on Space Debris, ESOC. ESA SP-473 (2001)

22. Sun, P., Colombo, C., Trisolini, M., Li, S.: Comparison of continuity equation and Gaussian mixture model for long-term density propagation using semi-analytical methods. Celest. Mech. Dyn. Astron. **134**(3), 22 (2022). https://doi.org/10.1007/s10569-022-10066-8

23. Sun, P., Colombo, C., Trisolini, M., Li, S.: Hybrid Gaussian mixture splitting techniques for uncertainty propagation in nonlinear dynamics. J. Guid. Control. Dyn. **46**(4), 770–780 (2023)

24. Sun, P., Li, S., Trisolini, M., Colombo, C.: Improved alpha shape-based continuum method for long-term density propagation. Celest. Mech. Dyn. Astron. Accepted on 25/10/2023. (2023) https://doi.org/10.1007/s10569-023-10171-2

25. Trisolini, M., Colombo, C.: Propagation and reconstruction of reentry uncertainties using continuity equation and simplicial interpolation. J. Guid. Control. Dyn. **44**(4), 793–811 (2021). https://doi.org/10.2514/1.G005228

26. Wittig, A., Colombo, C., Armellin, R.: Long-term density evolution through semi-analytical and differential algebra techniques. Celest. Mech. Dyn. Astron. **128**(4), 435–452 (2017). https://doi.org/10.1007/s10569-017-9756-x

27. Wittig, A., Di Lizia, P., Armellin, R., Makino, K., Bernelli-Zazzera, F., Berz, M.: Propagation of large uncertainty sets in orbital dynamics by automatic domain splitting. Celest. Mech. Dyn. Astron. **122**(3), 239–261 (2015). https://doi.org/10.1007/s10569-015-9618-3